



Article

Impact of Silicon Content and Particle Size in Lithium-Ion Battery Anodes on Particulate Properties and Electrochemical Performance

Jannes Müller ^{1,2,*}, Peter Michalowski ^{1,2} and Arno Kwade ^{1,2}

¹ Institute for Particle Technology, Technische Universität Braunschweig, Volkmaroder Str. 5, 38104 Braunschweig, Germany; p.michalowski@tu-braunschweig.de (P.M.); a.kwade@tu-braunschweig.de (A.K.)

² Battery LabFactory Braunschweig, Technische Universität Braunschweig, Langer Kamp 19, 38106 Braunschweig, Germany

* Correspondence: jannes.mueller@tu-braunschweig.de

Abstract: Silicon (Si) is considered a promising anode active material to enhance energy density of lithium-ion batteries. Many studies have focused on new structures and the electrochemical performance, but only a few investigated the particulate properties in detail. Therefore, a comprehensive study on the impact of Si content (5, 10, 15 wt.%) and particle size (120, 160, 250 nm) of core–shell structured Si@Gr composites on particulate and electrode properties was conducted. It was shown that both parameters had significant impact on the specific surface area (SSA) of particles, which was later correlated to the initial capacities and coulombic efficiencies (ICEs). Furthermore, changes in pore size distribution and electrical conductivity were found. The built full cells showed high initial capacities ($>150 \text{ mAh g}^{-1}$), good rate capability (75% at 1 C, 50% at 2 C) and ICEs (>80%). The energy density was found to increase by 32% at 15 wt.% Si compared to graphite (Gr), indicating the future potential of Si. In addition, the impact of a carbon coating was investigated (Si@Gr/C), which led to a reduction in SSA, improved particle stability and higher capacity retention. Consequently, this study emphasizes the importance of also investigating the particulate properties of Si anodes.



Citation: Müller, J.; Michalowski, P.; Kwade, A. Impact of Silicon Content and Particle Size in Lithium-Ion Battery Anodes on Particulate Properties and Electrochemical Performance. *Batteries* **2023**, *9*, 377. <https://doi.org/10.3390/batteries9070377>

Academic Editor: Wilhelm Pfleging

Received: 14 June 2023

Revised: 4 July 2023

Accepted: 11 July 2023

Published: 13 July 2023



Copyright: © 2023 by the authors. Licensee MDPI, Basel, Switzerland. This article is an open access article distributed under the terms and conditions of the Creative Commons Attribution (CC BY) license (<https://creativecommons.org/licenses/by/4.0/>).

1. Introduction

Since their commercialization, lithium-ion batteries have become the main rechargeable energy source for mobile devices and electric vehicles. Electric mobility is considered as the future form of mobility, but the specific energy (Wh kg^{-1}) and energy density (Wh L^{-1}) are crucial parameters for its success. As the specific energy is calculated by the specific capacity and the operating voltage, new active materials with high specific capacities and acceptable low operating voltage for the anode or high operation voltage for the cathode are needed.

On the anode side, the commonly used graphite (Gr) exhibits a theoretical capacity of 372 mAh g^{-1} (LiC_6) [1]. Due to great research effort in recent years, this theoretical value is almost reached in practice. Therefore, research and industry increasingly focus on new active materials like silicon (Si), which has the highest known specific capacity of about 4200 mAh g^{-1} ($\text{Li}_{21}\text{Si}_5$) of possible anode materials [2]. Even though only 3579 mAh g^{-1} ($\text{Li}_{15}\text{Si}_4$) can be reached at room temperature [3], its specific capacity is still ten times higher than that of Gr.

However, a wide commercial usage of Si as an anode material in lithium-ion batteries has not taken place yet. The reason for this is the volume change of up to 300% of the initial particle volume [4,5], which may lead to particle breakage (pulverization) [6,7], defects

in the electrode structure and continuous SEI growth [8]. The solid electrolyte interphase (SEI) is formed within the first cycle on the surface of the anode particles, as the electrolyte is not electrochemically stable in the voltage window of the anode [8]. For Gr particles, which exhibit only a small volume expansion of 10% during lithiation [9], the SEI can maintain its structure. In contrast to this, the SEI is broken up within every cycle for Si, so the new electrolyte decomposes on the anode surface [10,11]. As a result, the cell dries up over time and continuous SEI growth takes place, which both lead to an increase in ionic resistance. In addition to that, the SEI build-up consumes lithium [12]. Furthermore, the low electrical conductivity of Si leads to limited rate capability and may provoke an incomplete delithiation and higher irreversible lithium loss [13,14].

In order to overcome the structural problems, the volume expansion of Si needs to be lowered or buffered. One common approach for this is the decrease in Si particle size [15–18]. Even though the relative volume change is the same, the absolute volume change is smaller and, thus, enables a better electrode and SEI stability. In the literature, a critical particle size of 150 nm is often stated, below which no particle breakage occurs [19,20]. However, the usage of Si nanoparticles (NPs) is typically accompanied by an increase in the specific surface area, which is linked to the initial capacity loss and the SEI growth [17,21,22].

Therefore, when using Si NPs, the surface area needs to be minimized. This can be achieved through functional coatings on top of the Si NPs [23], i.e., carbon [21,24–26]. Carbon coatings have the additional advantage that they are ionically and electrically conductive [26,27]. Besides that, carbon coatings are flexible and can help to maintain the particulate structure during cycling [18,24,28] or during critical process steps, for instance, during calendering [24,29]. However, it needs to be considered that the coating is an additional inactive component and thus reduces the overall energy density and specific energy [30].

The combination of small amounts of Si with carbon materials like Gr is also a common approach to improve the cycle life of Si containing anodes [31–34]. Gr with its high electrical conductivity, high reversibility and low volume expansion can provide a stable and conductive matrix and thus improves cycle life. However, an inhomogeneous distribution of Si within the Gr matrix might lead to local high stresses and poor electrochemical performance. Therefore, in a previous study core–shell structured Si@Gr and carbon coated Si@Gr/C composites with evenly distributed Si NPs have been developed [24,28]. The particle structure is similar to the raw Gr, so that no changes in electrode production are necessary and the same porous electrode structure of conventional Gr anodes can be maintained.

Within this study, the impact of Si particle size (120, 160, 250 nm) and Si content (0, 5, 10, 15 wt.%) of Si@Gr and Si@Gr/C composites are investigated in more detail. In the literature, the variation of Si content and Si particle size is not a new topic as it was studied multiple times [32,35–37]. However, almost all studies focused solely on the electrochemical performance and did not study the particulate properties or try to link these to the electrochemical performance. Therefore, this publication focuses on the structural and electrical properties of the composite particles. Nevertheless, a detailed electrochemical study is also conducted.

2. Materials and Methods

The process route for the production of Si@Gr and Si@Gr/C composite particles and electrodes was already established in our previous publication [24,28]. This included the nanogrinding of Si, the subsequent preparation of core–shell-like Si@Gr composites via fluidized bed granulation (FBG) as well as a pitch derived carbon coating (Si@Gr/C). Electrode production was carried out using a continuous pilot scale coating machine. As the aim of this work was not to study the influence of process parameters but the particulate properties, all process parameters were held constant compared to the previous work. Consequently, only changes to the previous work will be highlighted within this

experimental section. For further details about the process route and parameters, refer to [24].

2.1. Preparation of Si@Gr and Si@Gr/C Composite Particles

Within this work, Si@Gr composites with different Si contents and Si particle sizes were produced, from which some were also carbon coated (Si@Gr/C). An overview of the different materials is given in Table 1. For a constant particle size of around 120 nm, the Si content was varied from 0–15 wt.% (0, 5, 10, 15 wt.%), where 0 wt.% corresponds to pristine Gr. Furthermore, a variation of the Si particle size (120, 160, 250 nm) was conducted at a constant Si content of 10 wt.%. The 120 nm and 160 nm Si@Gr composites were additionally carbon coated.

Table 1. Overview of different samples with variation in Si content, Si particle size and pitch coating.

#	Si Content m_{Si}	Theor. Capacity	Si Particle Size x_{Si}	Carbon Coating
	wt.%	mAh g^{-1}	nm	-
1	0.0	360	-	-
2	5.0	450	117	-
3			117	-
4			117	Yes
5	10.0	600	160	-
6			160	Yes
7			250	-
8	15.0	750	118	-

2.1.1. Grinding of Si Particles

The nanogrinding of Si was carried out with a stirred media mill operated in circuit mode and with ethanol as solvent. As raw material, micron-sized Si ($x_{50,3} = 17.1 \mu\text{m}$) from PyroPowders (Grammetal, Germany) was used. A detailed description of parameters and setup can be found in [24,38]. In contrast to the previous work, the Si was ground to different particle sizes (120 nm, 160 nm, 250 nm). For each target particle size, a separate experiment using a size-dependent grinding time was conducted. The particle size reached is presented Figure S1 as a function of the specific energy input during grinding. In order to reach particle sizes of 250, 160 and 120 nm, energy inputs of about 20,000, 36,000 and 58,000 kJ kg^{-1} were needed, respectively.

2.1.2. Fluidized Bed Granulation (FBG)—Preparation of Si@Gr

For the preparation of the Si@Gr composites, a fluidized bed granulator (FBG) was used [24]. The ground Si suspension was sprayed into the process chamber, in which artificial Gr particles ($x_{50,3} = 17.1 \mu\text{m}$) were fluidized. Within the process, a core–shell structured Si@Gr composite particle (Gr core and Si shell) was formed. In order to produce composites with different Si contents, more Si suspension was sprayed in and, thus, the process time was extended.

2.1.3. Carbon Coating and Carbonization—Preparation of Si@Gr/C

The carbon coating was carried out by dry mixing 10 wt.% of HSP pitch from China Steel Chemical Corporation (Kaohsiung City, Taiwan) with the Si@Gr composites and then carbonizing this mixture in crucibles in a chamber furnace for 2 h at 900 °C. In our previous study, an agglomeration during heat treatment was observed, which necessitated a sieving step before electrode production [24]. Therefore, the Si@Gr/C composites were sieved to a fineness of <50 μm using an air jet sieve.

2.2. Electrode Production

For electrode production, the composite particles were dry mixed with carboxymethyl cellulose (CMC) binder (Walocel CRT 2000 PA 09 from DuPont, Wilmington, NC, USA) and carbon black (Super C65 from Imery Graphite and Carbon, Paris, France). As a next step, this mixture was dispersed in deionized water for 45 min at a tangential speed of 9 m s^{-1} . After this, styrol butadiene rubber (SBR) binder (BM-451B from Zeon Europe, Düsseldorf, Germany) was added and the suspension was dispersed for an additional 10 min at 3 m s^{-1} . The suspension was degassed and cooled to 15°C throughout the whole experiment. The final slurry consisted of 90 wt.% active material, 3.6 wt.% CMC, 1.8 wt.% SBR, 1.4 wt.% carbon black at an overall solids content of 40 wt.%. For more information about the dispersing process, refer to [24].

The prepared slurry was then coated onto copper foil from Furukawa Electric (Tokio, Japan) using a continuous coating and drying machine from Kroenert GmbH (Hamburg, Germany) to obtain an areal capacity of 3 mAh cm^{-2} [24]. The mass loadings for the different Si contents (0, 5, 10, 15 wt.%) of Si@Gr were as follows: 9.26, 7.41, 5.56, 4.44 mg cm^{-2} . Si@Gr/C (always 10 wt.% Si) was coated with a higher areal loading of 6.17 mg cm^{-2} , because at such high silicon contents the capacity contribution of the carbon coating can be neglected [24] and it was thus considered as inactive material. The anodes were used uncalendered.

The cathode slurry was prepared in a planetary mixer and comprised 95.5 wt.% NMC622 (HED from BASF, Ludwigshafen, Germany), 2.25 wt.% polyvinylidene fluoride (PVDF) binder (Solef 5130 from Solvay, Brussels, Belgium), 1.5 wt.% carbon black (Super C65 from Imerys Graphite and Carbon, Paris, France) and 0.75 wt.% conductive graphite (SFG6L from Imerys Graphite and Carbon, Paris, France). The slurry was coated onto aluminum foil to an areal capacity of 3 mAh cm^{-2} (18.26 mg cm^{-2}) using again the pilot-scale coating and drying machine. Finally, the cathode was calendered to a density of 3 g cm^{-3} .

2.3. Characterization

2.3.1. Particle Analysis

The particle analysis included a measurement of the particle size distribution and the specific surface area (SSA) as well as a thermogravimetric analysis (TGA). The particle size measurement was carried out with an LA960 laser scattering device from Horiba (Kyoto, Japan). During the measurement, ultrasonic stress was applied by a sonotrode installed in the device.

The SSA was measured via the BET method using a Nova 2000e analyzer from Quantachrome (Boynton Beach, FL, USA) and nitrogen as an analysis gas. In order to reduce moisture, the particle samples were dried for 6 h at 50°C beforehand. For each material, two measurements were conducted. The theoretical calculation of the SSA based on particle shape is shown in Equations (S3)–(S9).

TGA measurement was carried out using a TGA/DSC1 analyzer from Mettler Toledo (Gießen, Germany). As an analysis gas oxygen at flow rate of 60 mL min^{-1} was used. The heating rate and maximum temperature were $10 \text{ }^\circ\text{C min}^{-1}$ and $1100 \text{ }^\circ\text{C}$, respectively.

2.3.2. Electrode Analysis

The pore size distribution of the electrodes was measured via mercury intrusion using a PoreMaster 60 porosimeter from Quantachrome (Boynton Beach, FL, USA). During measurement, mercury is inserted in the pores by applying an external pressure, which relates to the pore size. More information about the measurement procedure can be found in Froboese et al. [39].

The electrical conductivity of electrodes was investigated by applying a current of 10 mA to an electrode die cut (diameter: 12 mm) and measuring the voltage drop. In order to ensure good contact of the brass stamps to the electrode surface, the electrodes were

compressed with 40 N. More information about the measurement procedure can be found in Haselrieder et al. [40].

Pictures of electrode cross sections were taken with a Phenom XL scanning electron microscope from ThermoFisher Scientific (Waltham, MA, USA). As a detector, a backscattered electron detector (BSD) operated at 10 kV was used.

2.3.3. Electrochemical Characterization

The electrochemical analysis was carried out in PAT test cells from EL-Cell (Hamburg, Germany), which enabled a three-electrode testing setup. As a separator, a double-layered polypropylene (PP)/polyethylene (PE) separator with a lithium reference ring was used. Both electrodes had a diameter of 18 mm and an areal capacity of 3 mAh cm^{-2} . The electrolyte comprised 1 M LiPF₆ in EC/EMC (3/7 wt.%) with 2 wt.% vinylene carbonate (VC) and 10 wt.% fluoro ethylene carbonate (FEC). The cycling was performed with a CTS-LAB battery tester from BaSyTec (Asselfingen, Germany). The cycling was always performed symmetrically (same C-rates for charging and discharging) and in constant current (CC) mode without a constant voltage step. The cycling procedure included four formation cycles, a rate capability test and a long-term cycling test for additional 100 cycles. The rate capability test was carried out with three cycles for each C-rate (0.2 C, 0.5 C, 1 C, 2 C). Before subsequent long-term cycling, three recovery steps of 0.1 C were carried out to evaluate the aging after rate capability testing. The long-term cycling test was carried out as two sets of 50 cycles at 0.5 C with two intermediate recovery cycles at 0.1 C for capacity check-up. For full cells, the voltage window was 2.9–4.2 V.

The voltage window of the anode half cells was 0.01–0.9 V vs. Li/Li⁺. In contrast to typical half cells, which are cycled against a lithium metal counter electrode, the anode was cycled against a lithium reference electrode. To serve as a stable lithium source, an oversized cathode was used as the counter electrode. This was carried out to avoid unstable cycling that may occur with lithium metal. This setup was already described in our previous publication [24].

The specific energy (Wh kg^{-1}) and energy density (Wh L^{-1}) were calculated based on the electrode weights and heights. For this, both anode and cathode and half of the substrates were considered. The reason for taking only half of the substrate into account is that in larger multilayer cells double side coated electrodes would be used. As the separator was preassembled with the lithium reference in a casing and about 220 μm thick, it was neglected for the calculation. The electrolyte was used in excess and therefore also neglected. For the electrode weight, the overall coating mass of the electrode was taken as a basis. The electrode volume was calculated by multiplying the electrode area (diameter: 18 mm, area: 254.47 mm^2) with the electrode height. The equations used are given in Equations (S1) and (S2).

3. Results and Discussion

3.1. Material Properties of Si@Gr and Si@Gr/C Composites and Electrodes

In order to understand the electrochemical performance, it is critical to characterize both the electrode structure and the particulate properties of the composites. These include, in particular, the particle size distribution, the chemical composition, the specific surface area and the electrode porosity.

The particle size distribution of the pristine Gr (0 wt.% Si) and Si@Gr composites with three different Si contents of 0, 5, 10 and 15 wt.% is given in Figure 1a. Pristine Gr exhibits a sharp distribution with a median particle size of $x_{50,3} = 18.1 \mu\text{m}$ and no particle fraction $<5 \mu\text{m}$ or $>40 \mu\text{m}$. In contrast to this, the particle size distribution broadens with increasing Si content and a particle size fraction below 1 μm arises. The increase in particle size is related to the agglomeration of Gr and Si particles with increasing process time. The appearance of particles $<1 \mu\text{m}$, however, is caused by the instability of the Si@Gr composites and the detachment of Si NPs from the Gr surface. With increasing Si content,

this particle size fraction increases significantly, indicating that increasingly more silicon is not firmly attached to the Gr surface.

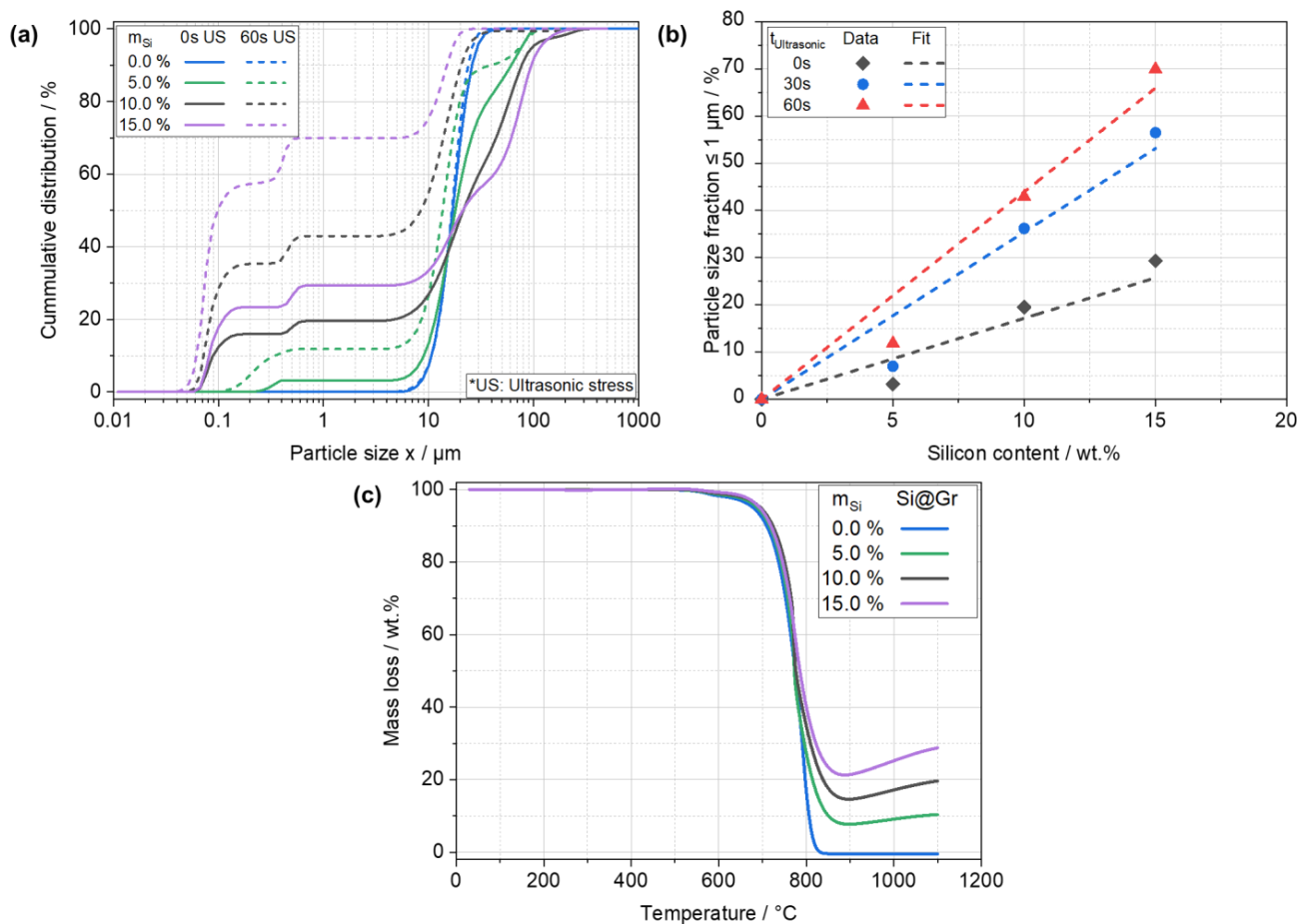


Figure 1. (a) Particle size of Si@Gr composites with different silicon contents without (0 s US) and with (60 s US) ultrasonic treatment (US) during particle size measurement; (b) detachment of silicon nanoparticles calculated based on the particle size fraction $< 1 \mu\text{m}$ as a function of silicon content and US time; (c) thermogravimetric analysis as a function of silicon content.

As it is difficult to evaluate the composite stability during slurry production, especially because the particle size of carbon black is similar to that of the Si NPs, the stability was measured indirectly by applying 30 and 60 s of ultrasonic stress to the samples during particle size measurement. Even though this is not directly comparable to the actual shear stress during dispersing, it can give a first impression of the stability. As expected, the ultrasonic treatment results in an even more pronounced detachment of Si NPs and indicates that the initial aimed structure might not be maintained during electrode production. In Figure 1b the particle size fraction $< 1 \mu\text{m}$ (free Si NPs) is plotted as a function of the silicon content for three ultrasonic stressing times (0, 30, 60 s). With increasing Si content, the amount of detached, i.e., free, Si NPs increases linearly. However, the values for 5 wt.% Si are smaller than expected and do not fit in the linear trend. This might be related to the possibility that a certain amount of Si can firmly attach to the Gr surface. If more Si NPs are added, these may only be loosely or not attached to the Gr surface. It is noteworthy that an improvement in composite stability after carbon coating was already demonstrated in our previous publication [24].

Within the fluidized bed process, some of the Si suspension sticks to the walls, filters and sieve plate, so the real Si content of the composites might differ from the theoretically calculated value. Therefore, thermogravimetric analysis (TGA) is used to determine the real silicon content and the results for Si@Gr composites with varying Si content are given in

Figure 1c. During the measurement, the sample is heated under oxygen atmosphere, which leads to the complete decomposition of Gr (0 wt.% Si) above 800 °C. The Si containing Si@Gr composites, however, show a local minimum followed by a mass increase and a plateau at 1100 °C. This mass increase is related to the formation of SiO₂ at higher temperatures. Based on the final values of 10.39, 19.63 and 28.75 wt.% and taking into account the molecular weight ratio of Si and SiO₂, the overall Si content for 5, 10 and 15 wt.% Si can be calculated to 4.85, 9.16 and 13.42 wt.% Si, respectively. All values are slightly lower than the theoretical values. To simplify the following results, only the theoretical values of 5, 10 and 15 wt.% are used.

The results of TGA for the Si@Gr composites with varying Si particle size and Si@Gr/C composites with carbon coating are given in Figure S2. It can be seen that the variation in particle size has only minor influence on the results. In contrast to this, the existence of a carbon coating for Si@Gr/C composites is clearly evident, as an additional weight loss starting at around 500 °C occurs, which we attribute to the oxidation of the carbon coating. Apart from that, the curve is similar in shape to the others.

The specific surface area (SSA) is an important parameter for anode materials as it is related to the initial capacity loss. Besides that, it is also linked to the capacity loss during cycling, in particular, for Si anodes. Therefore, the SSA of Si@Gr composites as a function of Si content and Si particle size is given in Figure 2. At a constant Si particle size of 120 nm, the SSA as a function of the Si content shows a linear correlation (Figure 2a), it changes from 2.89 m² g⁻¹ for pristine Gr to 6.76, 10.06 and 13.10 m² g⁻¹ for 5, 10 and 15 wt.% Si, respectively.

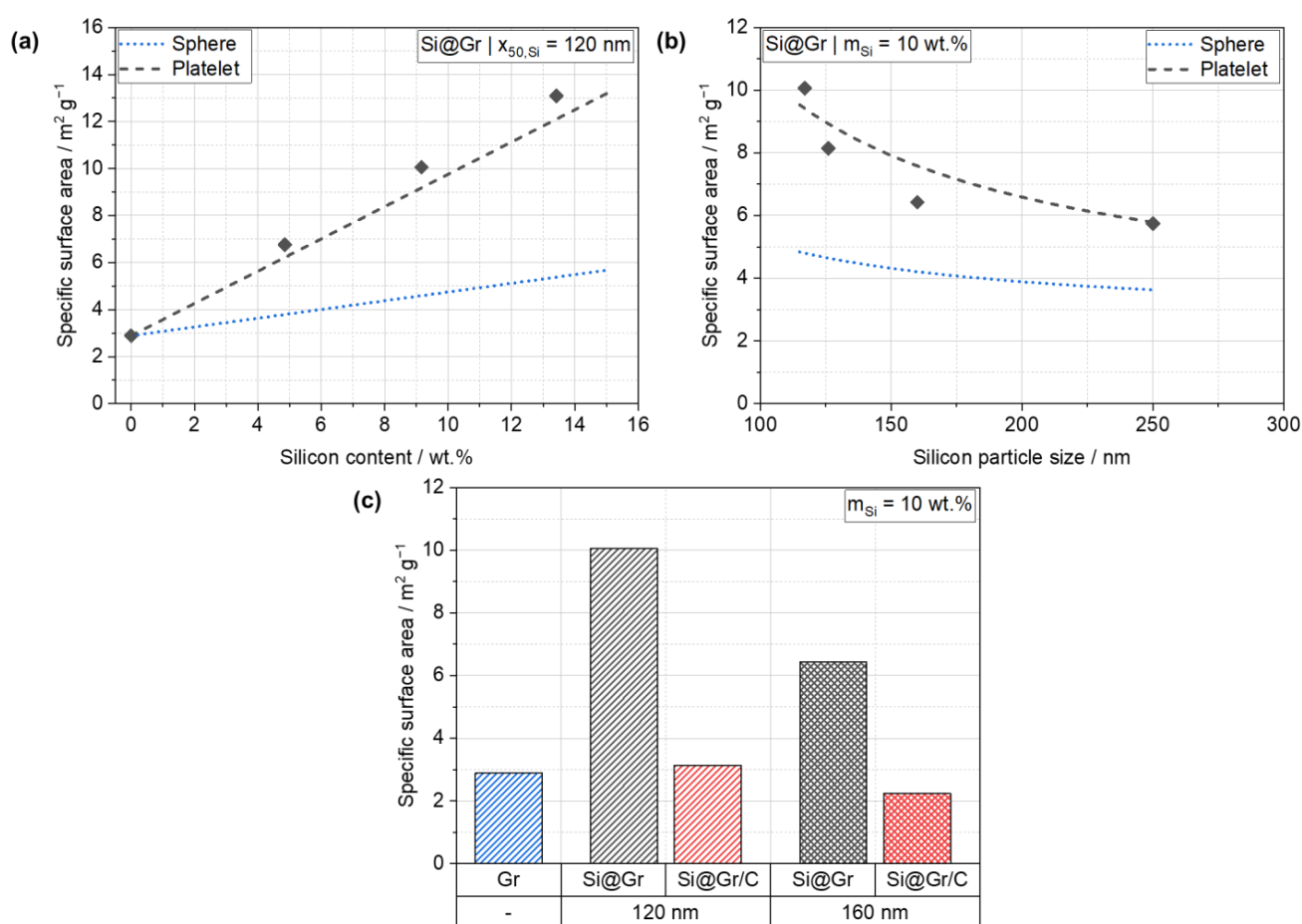


Figure 2. Specific surface area as a function of Si content (a) and Si particle size (b). In (a,b), the theoretically calculated values for spherical (dashed line) and plate-like shaped particles with a diameter to height ratio of 8:1 (dotted line) are also plotted. (c) Specific surface area before and after carbon coating (m_{Si} = 10 wt.%).

In Figure 2b, the SSA is plotted against the Si particle size at a constant Si content of 10 wt.%. It can be seen that a decrease in Si particle size results in an exponential increase in the SSA. This behavior counteracts the improved electrochemical performance caused by the decrease in absolute volume expansion with decreasing particle size. A larger SSA may lead to more side reactions as it is linked to the SEI growth, which is continuously taking place in unstructured Si anodes.

As clear trends for the SSA could be observed, it was tried to find a method to describe or even predict the resulting SSA at certain Si contents and Si particle sizes. Therefore, theoretical calculations based on the amount of Si content and Si particle size were conducted. Starting from the total volume of Si particles and the amount of Si particles in the sample, the theoretical SSA for spherical Si particles at certain Si contents and Si particle sizes can be calculated. The results are plotted in blue in Figure 2a,b. It can be seen that the calculated values always underestimate the measured data, especially at higher Si contents and smaller Si particle sizes. In order to obtain a better correlation, the real shape of the particles needs to be taken into account. As already noticed in previous publications [28,38], the ground Si NPs exhibit a platelet shape with larger extent in width than in height. Consequently, a cylindrical shape with a larger diameter than height is used as a basis for the calculation. A diameter to height ratio of 8:1 shows promising results. Within the range of measured data points, the theoretical values are in good agreement with the measured data, particularly for the variation of Si content. However, for the variation of Si particle size an even steeper increase in the measured data is observed. Despite this, the calculated values can still give a good first way to describe the SSA within the measured range. For even smaller Si particles, this model may exhibit too high deviation.

In Figure 2c, a comparison between the pristine Si@Gr and the carbon coated Si@Gr/C composite particles at a constant Si content of 10 wt.% is given. The positive effect of the pitch derived carbon coating is clearly visible. For composites with 120 nm Si NP size, the SSA is reduced from $10.06 \text{ m}^2 \text{ g}^{-1}$ to $3.14 \text{ m}^2 \text{ g}^{-1}$, which is close to the value of pure Gr ($2.89 \text{ m}^2 \text{ g}^{-1}$). As previously determined, a strong dependency of the SSA on the particle size is also apparent here. For a Si particle size of 160 nm, the SSA can be reduced even below the value of pristine Gr ($6.43 \text{ m}^2 \text{ g}^{-1}$ to $2.24 \text{ m}^2 \text{ g}^{-1}$). Therefore, a carbon coating can help to significantly reduce the active surface area and should thus reduce the initial SEI losses.

In addition to the particulate properties, an understanding of the electrode structure can give further insight into the processes during operation. Here, one important factor is the pore size distribution, which is shown in Figure 3a,b. Two peaks in the pore size distribution can be noted, one from 1–10 μm and one below 1 μm . The peak in the coarser pore size range is related to the active material. With increasing Si content, this peak diminishes and nearly disappears at 15 wt.% Si (Figure 3a). This behavior is most likely caused by free Si, which has detached and is now filling the pores between the coarser Gr or composite particles. This accumulation of Si within the pores might cause some problems during cycling, as the volume expansion is locally pronounced within this region. The second peak is usually attributed to the pores of carbon black, so no significant change should be observable between pristine Gr and Si@Gr anodes. However, distinct differences between the two materials can be noted. While for Gr a broad peak from 0.1–1 μm is visible, this peak shifts towards smaller pore sizes for Si@Gr composites. The Si NPs are in the same particle size range and are likely the reason for this. As this peak is reproducible for all Si contents, this might relate to the fixed silicon on the surface of the Gr particles. For the variation of Si particle size (Figure 3b), only a slight shift to coarser pore sizes with increasing Si particle size can be recognized.

However, with carbon coating (Si@Gr/C), the active material peak is enlarged and shifts towards coarser pore sizes. This shift is caused by the fact that the particle size increases after carbon coating [24]. The enlargement of the peak height means that more pores are present in this pore size range. In contrast to the Si@Gr electrode, in which the pores are filled with free Si NPs and the peak height diminishes, the carbon coating can

stabilize the composite structure and inhibit the detachment of Si NPs. The hypothesis that the peak in the smaller pore size region might relate to the fixed Si NPs is further underlined by the fact that it almost diminishes after carbon coating. The smallest peak $<0.03 \mu\text{m}$ is only visible after carbon coating and could be related to an inner porosity of the carbon coating or to measuring artefacts.

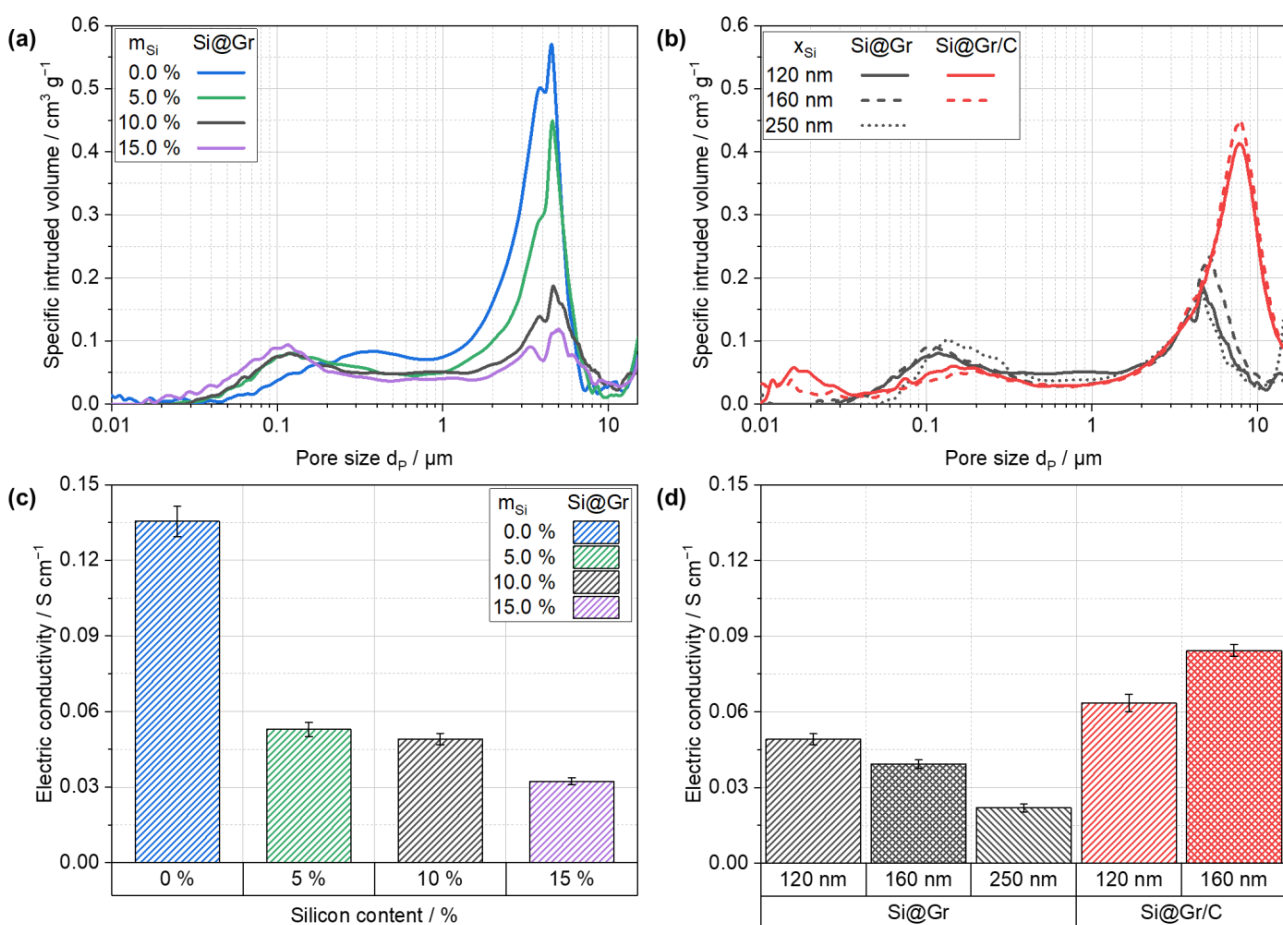


Figure 3. Structural electrode properties: (a) Pore size distribution of Si@Gr anodes as a function of Si content; (b) pore size distribution of Si@Gr and Si@Gr/C anodes as a function of Si particle size; (c) electrical conductivity of Si@Gr anodes as a function of Si content; (d) electrical conductivity of Si@Gr and Si@Gr/C anodes as a function of Si particle size.

Another parameter, which relates to the structural properties and can be detected, is the electrical conductivity of electrodes. The results of such measurements are depicted in Figure 3c,d. As expected, the highest electrical conductivity can be obtained for Gr, while a decline is evident for the Si containing Si@Gr electrodes (Figure 3c). This can be explained by the lower intrinsic electrical conductivity of Si. Even though the measured values are lower, an electrical limitation is not expected, because the values are still relatively high in relation to the ionic resistances [41,42]. However, during operation the low electrical conductivity of Si can locally lead to inhomogeneous or even incomplete delithiation, causing a loss of active lithium, especially in places with locally more Si. For the variation of particle size, no change was expected. However, a decrease in the electrical conductivity with increasing particle size is evident. The reason behind this phenomenon remains unclear to this point and necessitates further investigation. After carbon coating, an increase in the electrical conductivity can be noted, which is in good accordance with the expectations, because the amorphous carbon coating is highly conductive. In conclusion, the measurement of the electrical conductivity of anodes provides an easy way to detect structural differences.

3.2. Electrochemical Performance

The electrochemical measurements were performed in small test cells (PAT cells from EL-Cell GmbH, Hamburg, Germany) with an electrode diameter of 18 mm against an NMC 622 cathode. For all produced anodes, full cells were built and tested in a symmetrical rate capability test up to 2 C without a constant voltage (CV) step. Subsequently, a symmetrical long-term cycling test at 0.5 C with inserted recovery steps at 0.1 C after 50 cycles was carried out. In order to differentiate whether the electrical performance was related to the anodes or the full cell setup with a limited amount of lithium, some half cells were also built. For this, the Si@Gr and Si@Gr/C composites with a Si content of 10 wt.% and a Si particle size of 120 nm were chosen.

The specific discharge capacity (related to the mass of the active material of the anode) of the half cells (with 10 wt.% Si) as a function of the C-rate is shown in Figure 4a. The Si@Gr and Si@Gr/C anodes reach initial specific capacities of 612.6 and 674.0 mAh g^{-1} , respectively, which is close to the theoretical capacity of about 600 mAh g^{-1} . Furthermore, the cells show high initial coulombic efficiencies (ICEs) of 84.1 and 86.0%, respectively. The higher ICE of the carbon coated material could be caused by the reduction in SSA (Figure 2c). Besides that, the carbon coated Si@Gr/C composite anodes consistently exhibit higher capacities than the uncoated Si@Gr. This may be related to the lithium storage capacity of the pitch coating, which has been discussed in our previous work [24]. In the further course, both anodes show good rate capability, reaching 448.4 and 508.9 mAh g^{-1} at 1 C, which relates to 73.2 and 75.5% of the initial capacity. At a C-rate of 2 C, values of 266.7 (43.5%) and 334.0 mAh g^{-1} (50.0%) are obtained. In the subsequent recovery step again at 0.1 C, the specific capacities obtained (606.6 and 681.2 mAh g^{-1}) reached their initial values. Consequently, no visible aging took place during the rate capability test. The coulombic efficiency shows some fluctuations in the beginning, which is related to the change in the C-rate. Nevertheless, a strong trend towards 100% is evident within the long-term cycling test. With regard to the capacity, the trend of higher capacities of the carbon coated Si@Gr/C is prolonged during the long-term cycling test (Figure 4b). However, a slightly unsteady cycling behavior is apparent. This behavior might be related to side reactions of the lithium reference electrode, but the exact reason cannot be distinguished from these data. In contrast to this, Si@Gr shows a linear capacity fading in the beginning and only minor fluctuations in the end. The inserted recovery cycles (0.1 C) at cycle 72 and 123 reveal that at low C-rates most of the capacity can be retained. The relative capacities (normalized to the recovery cycles before the long-term cycling test (cycle 17)) are given in Figure S3. Even after 123 cycles, Si@Gr and Si@Gr/C show a capacity retention of 86.4 and 92.5%, respectively.

In summary, the anodes exhibit excellent cycling behavior in half cell configuration, as they reach high ICEs of >84%, initial capacities near their theoretical values ($>600 \text{ mAh g}^{-1}$), good rate capability (about 43–50% of initial capacity at 2 C) and high capacity retention after long-term cycling (up to 92% after 123 cycles). In addition to that, the positive effects of a carbon coating are clearly visible in the cycling data.

In a next step, full cells are built to test the anodes under more practical conditions. Again, rate capability and long-term cycling tests are performed to investigate the differences for a variation in Si content and Si particle size (Figure 5). As the limiting factor in full cells is the lithium amount of the cathode, in the following the specific discharge capacities refer to the mass of the cathode active material. Since the same cathode is used in all cells, all arising differences can be attributed solely to the anode (at a constant areal capacity of 3 mAh cm^{-2} for all compositions). Voltage curves of all built full cells at different cycles (all at 0.1 C) are shown in Figure S6. For the variation of Si content, which is shown in Figure 5a,b, the initial specific discharge capacities for 0, 5, 10 and 15 wt.% Si are 162.0, 158.6, 151.1 and 150.8 mAh g^{-1} , respectively. This means that with increasing Si content the achievable capacity decreases. This can be explained by the irreversible lithium loss in the first cycle. The ICEs follow the same trend with 85.7, 83.5, 82.9 and 80.4% for 0, 5, 10 and 15 wt.% Si, respectively. Lower ICEs mean higher lithium losses within the first charging

step and, thus, less free lithium is available within the following discharge step. A linear trend can be found for both the specific discharge capacity and ICE as a function of the SSA (Figures 2a and 5c). Within the first cycle, the build-up of the SEI takes place, which consumes lithium and is related to the surface area of the active material. As previously shown, a higher Si content leads to a linear increase in SSA and the same trend can also be found for the ICE and thus the discharge capacities. Hence, the structural properties of the composite particles can be directly related to the electrochemical performance (Figure 5c).

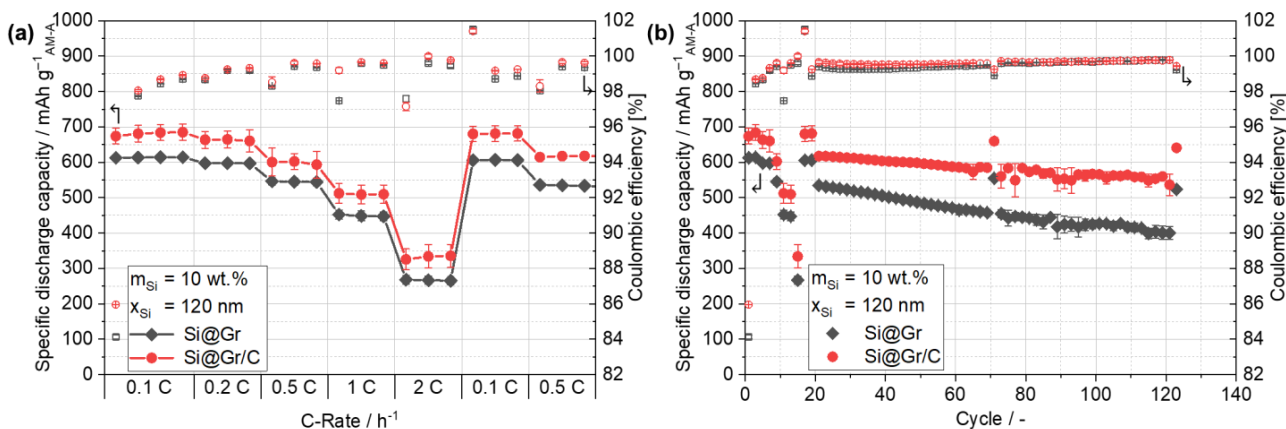


Figure 4. Electrochemical performance of Si@Gr and Si@Gr/C anodes ($m_{\text{Si}} = 10 \text{ wt.\%}$, $x_{\text{Si}} = 120 \text{ nm}$) in half cell configuration; (a) symmetrical rate capability test up to 2 C; (b) symmetrical long-term cycling at 0.5 C.

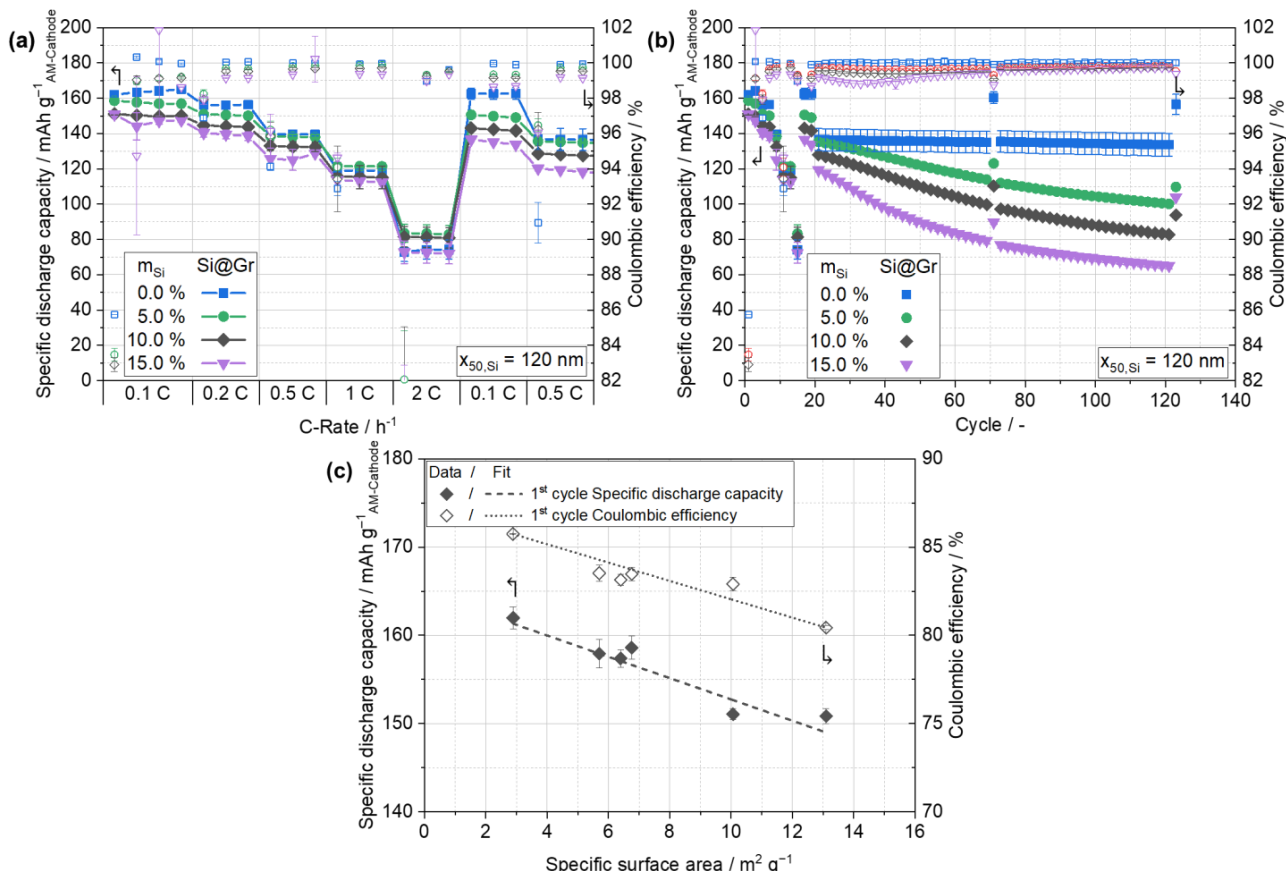


Figure 5. Electrochemical performance of Si@Gr in full cell configuration as a function of Si content: (a) Rate capability tests; (b) long-term cycling tests; (c) specific discharge capacity in the first cycle and initial coulombic efficiency (ICE) in the first cycle as a function of SSA.

Within the next cycles, a similar trend is evident, and anodes with higher Si contents show lower capacities. At C-rates of 1 C and 2 C, almost 75% and 50% of the initial capacities can be retained. This is in good accordance with the previous half cell results of 10 wt.% Si in Figure 4a. At a C-rate of 2 C, the cells with 5 and 10 wt.% Si exhibit higher specific capacities than pure Gr. This finding is in contrast to the previously obtained results and might be caused by the change in electrode height. When the areal capacity is kept constant, as carried out in this study, the mass loading and thus the electrode height decrease with higher Si content (Table S1). Therefore, a higher Si content relates to lower electrode thicknesses and shorter diffusion lengths for the Li-ions. This effect might not be dominant at low C-rates but gains in significance at high charging rates. Based on this, the achievable capacity for 15 wt.% should theoretically be even higher at higher C-rates, but this is not the case. Anodes with high Si contents suffer from more pronounced aging, as a larger surface area and larger volume expansion can lead to increased lithium consumption and the pores are blocked by free Si NPs. Therefore, the lithium loss within the previous cycles may have prevented a higher rate capability. In the subsequent recovery step (0.1 C), more distinct differences become visible. While the cells with pure Gr anodes show no capacity loss, the cells with 5, 10 and 15 wt.% Si suffer from 5.5, 5.8 and 10.3% capacity loss, respectively.

In long-term cycling, which corresponds to 123 cycles, distinct differences between Gr and Si@Gr cells can be distinguished (Figure 5b). Gr cells show nearly no capacity loss, so that even after 123 cycles, 96.7% of the initial capacity is still retained. In contrast to this, the Si@Gr cells suffer from severe capacity loss. For 5, 10 and 15 wt.% Si, capacity retentions of 81.7, 76.8 and 65.6% after 71 cycles and 72.9, 64.4 and 56.4% after 123 cycles are reached (Figure S4a), respectively. This again shows the obstacle in using higher silicon contents as it leads to increased SEI losses, higher volume expansion and thus structural changes in the electrode. The consequence of this is continuous lithium consumption. Compared to half cells, which have a nearly unlimited lithium reservoir, the amount of lithium in full cells is constricted by the amount of lithium stored in the cathode. Hence, in full cells a loss of active lithium is directly related to an overall capacity loss. This is also the reason for the differences to the half cell results in Figure 4b.

In order to study the impact of Si particle sizes, three different values are selected. As a critical particle size of 150 nm is often stated in the literature, a similar particle size of 160 nm was used as the standard size. Furthermore, one finer (120 nm) and one coarser fraction (250 nm) were also chosen. Based on literature data, distinct differences with better electrochemical performance for smaller Si particle sizes are expected. The initial discharge capacities follow the opposite trend, as values of 151.8, 154.6 and 156.5 mAh g⁻¹ are reached for 120, 160 and 250 nm. This might again be related to the larger SSA of composites with smaller Si particles (Figure 2b). However, this effect cannot be seen by the ICEs as the differences show no clear trend but are also within the standard deviation. In the following, only minor differences between the three particle sizes can be distinguished in the rate capability test (Figure 6a) and long-term cycling test (Figure 6b). After 123 cycles, capacity retentions of 64.4, 61.3 and 61.1% are reached (Figure S4b), respectively. This means that, indeed, a small improvement can be obtained for the smallest particle size, but larger differences were expected. As the capacity retention of 160 and 250 nm is nearly the same, the theory of a worsening in performance with increasing particle size cannot be confirmed for the investigated composite structure. Consequently, the particle size of Si might be not as important for anodes comprising mostly Gr with small amounts of Si. When larger Si particle sizes can be used, the grinding time and thus the energy consumption can be significantly reduced. By using only 250 nm instead of 120 nm, the energy consumption can be reduced by almost a factor of 3 (20,000 kJ kg⁻¹ vs. 58,000 kJ kg⁻¹, Figure S1).

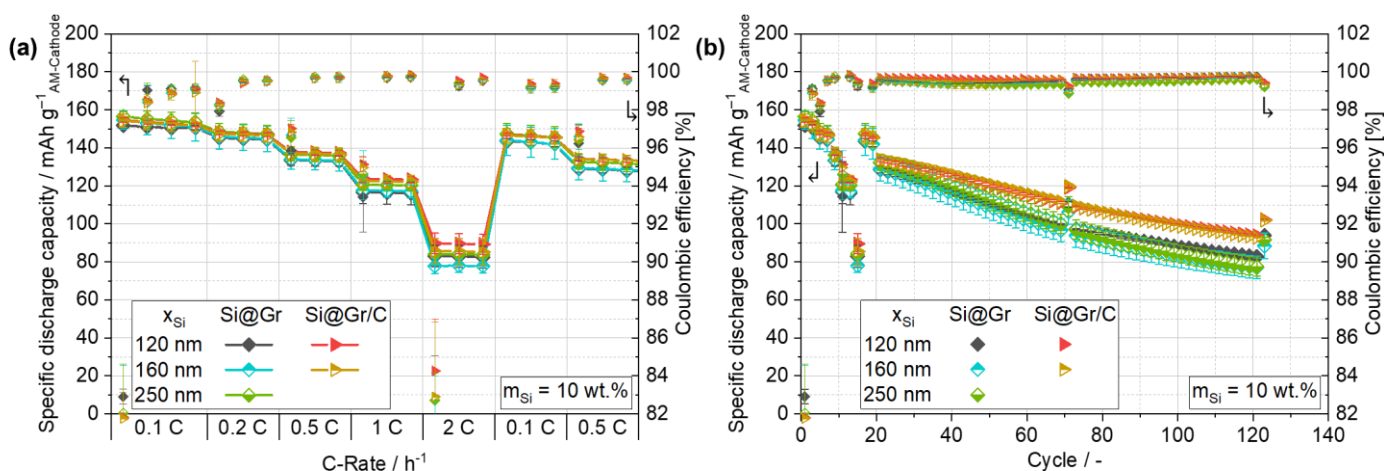


Figure 6. Electrochemical performance of Si@Gr and Si@Gr/C anodes in full cell configuration as a function of Si particle size: (a) Rate capability tests; (b) long-term cycling tests.

Next, the addition of a carbon coating is investigated, which is also shown in Figure 6. In comparison to the cells with the uncoated Si@Gr composite anode, the Si@Gr/C cells show only slight advantages in the rate capability test. Within the long-term cycling test, the positive impact of the carbon coating becomes clearer, because the capacity fading of Si@Gr/C is not as pronounced as for Si@Gr. Even though the differences seem to be small, the measured capacity retentions of 69.6 and 68.8% for Si@Gr/C composites with 120 and 160 nm, respectively, are about 8% larger than for Si@Gr. The reason for this small difference is the limited amount of lithium in the full cells, so that every lithium consumption process induces a capacity fade. Within half cells, a larger difference, especially in long-term cycling, is expected.

Based on these full cell results, the electrochemical performance of the prepared Si@Gr and Si@Gr/C composite materials is not sufficient for commercial applications and needs to be further optimized. However, it is important to show full cell results of Si containing electrodes, because the literature mainly focuses on half cells and non-scalable processes at the laboratory scale. Within this study, a correlation of the specific surface area of Si@Gr composites with the ICE and initial discharge capacity was found. Furthermore, it was shown that a reduction in particle size can have a positive impact on performance, but the effect is not that pronounced for Si@Gr anodes. Furthermore, it could be shown that Si containing anodes have the feasibility of using higher charging rates. In order to improve the performance, a further optimization of the carbon coating and particle structure is necessary. Moreover, a prelithiation could decrease the problem of lacking lithium in full cells.

After long-term cycling, the electrodes were washed inside a glovebox and SEM pictures were taken. In order to investigate the morphological changes, the SEM pictures of the cycled electrodes were compared to pristine ones. The resulting pictures are shown in Figure 7 and also in higher magnification in Figure S5. While for Gr almost no change in electrode height can be noted, the volume expansion of the Si containing anodes is clearly visible. The relative thickness increases in the anodes are 4.0, 27.0, 48.2 and 87.2% for Si@Gr with 0, 5, 10 and 15 wt.% Si (Table S1), which is again almost a linear increase. A higher Si content leads to more pronounced swelling of the electrode, which can cause electrical isolation, continuous SEI growth and pulverization of particles. All in all, this leads to increased degradation and capacity fading. Compared to the other electrodes, the particles within the Si@Gr/C electrode seem to be more spherical. This can only be caused by the pitch coating.

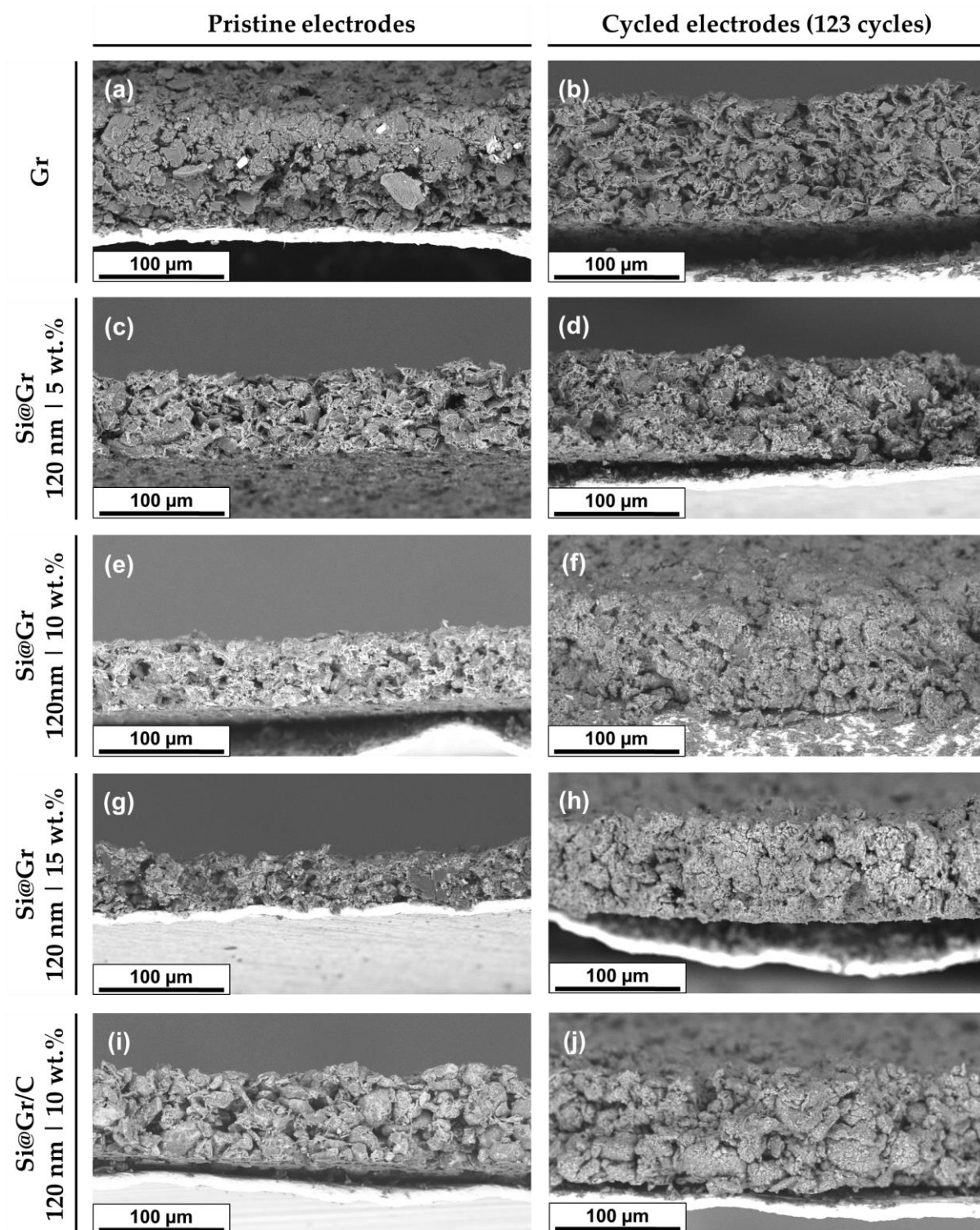


Figure 7. SEM images of Si@Gr and Si@Gr/C composite anodes before and after cycling for 123 cycles; (a,b) Gr; (c,d) Si@Gr, 5 wt.% Si, 120 nm; (e,f) Si@Gr, 10 wt.% Si, 120 nm; (g,h) Si@Gr, 15 wt.% Si, 120 nm; (i,j) Si@Gr/C, 10 wt.% Si, 120 nm.

Lastly, the specific energies (Wh kg^{-1}) and energy densities (Wh L^{-1}) of the full cells are calculated. In order to extend the range of electrical vehicles per battery charge, both parameters need to be increased. The replacement of Gr by Si is advantageous for both performance indicators. In the case of using anodes consisting mainly of Gr with small amounts of Si, as carried out in this study, the influence on energy density is more

pronounced than on specific energy. As only small cells with a preassembled separator, which incorporates a lithium reference, and an excess of electrolyte are used, both the separator and electrolyte are not considered within the calculation. Consequently, both the energy density and the specific energy solely refer to the electrodes (anode and cathode). Furthermore, only one half of the substrate is considered, because within multilayer cells the substrate would be coated on both sides.

The calculated energy densities are shown in Figure 8 at four different cycles (4, 18, 71, 122), which are all carried out at 0.1 C. As expected, the initial energy densities are enhanced from 552.1 Wh L⁻¹ for pure Gr to 619.5, 688.5 and 727.4 Wh L⁻¹ for higher Si contents (5, 10, 15 wt.% Si). This relates to a relative enhancement of about 32% at 15 wt.% Si. The reason behind this is the reduction in electrode thickness. As discussed before, when the silicon content is increased at a fixed areal capacity, the electrode thickness decreases. The measured electrode thicknesses can be found in Table S1. This improvement is, however, only present in the beginning. As already noted in Figure 5b, the Si containing electrodes suffer from severe capacity losses, causing a decline in energy density over cycling. In contrast to this, the energy density of Gr remains almost stable. In the end, this leads to the situation that the energy density of all Si@Gr cells has dropped below Gr. The variation of the Si particle size shows no real impact on the energy density (Figure 8b). Compared to Si@Gr cells, the additional carbon coating of Si@Gr/C leads to an initial decrease in energy density. This is related to the higher mass loading and thus electrode thickness. The carbon coating was considered as an inactive material, so that in order to achieve the same areal capacity, the mass loading was increased. Other than that, the same decline is visible as for the Si@Gr cells as the slightly better specific capacity (Figure 5c) is contradicted by the higher mass loading and electrode height.

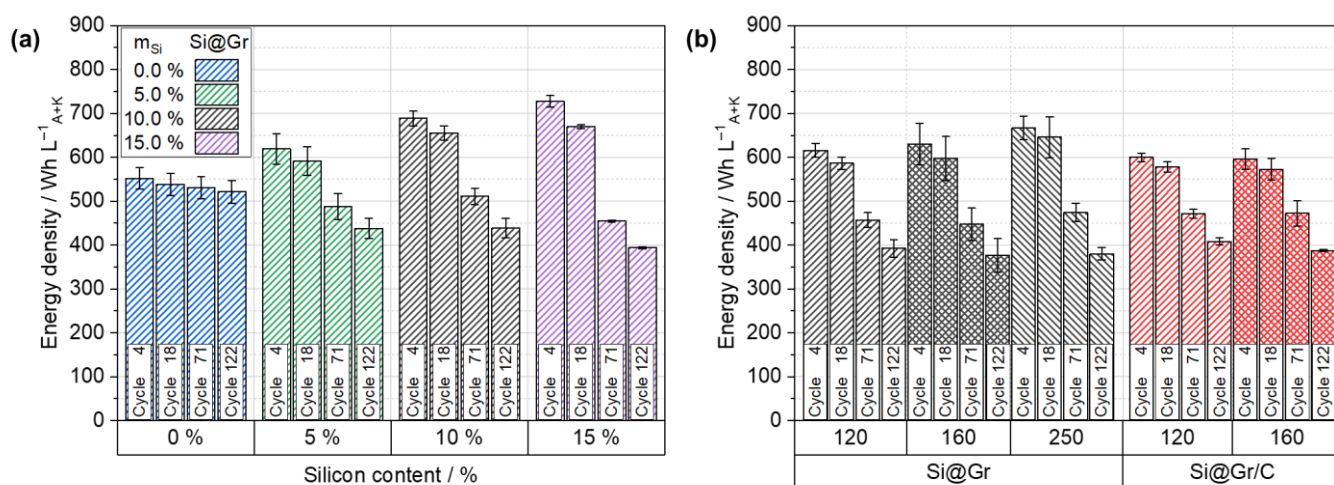


Figure 8. Energy density (Wh L⁻¹) at cycles 4, 16, 71 and 122 (all at 0.1 C) (a) of Si@Gr as a function of Si content for 120 nm Si NP; (b) of Si@Gr and Si@Gr/C as a function of Si particle size 10 wt.% Si.

For the specific energy, which is evaluated at the same cycles, no change in the initial values either by the variation of Si content, Si particle size or the addition of a carbon coating is evident (Figure S7). As previously mentioned, the anodes mainly consist of Gr with small amounts of Si (≤ 15 wt.% Si), so that the impact on the anode mass is not that pronounced. However, a higher Si content leads to a stronger decrease in specific energy during cycling. Even more important than the active mass of the anode is that of the cathode, which is about two times higher than the active mass of a pure Gr anode and even four times higher than for a Si@Gr anode with 15 wt.% Si. Hence, an optimization of the cathode mass has a larger impact on the specific energy than the anode and a mutual enhancement needs to be carried out for optimizing both energy density and specific energy.

4. Conclusions

Based on a previously developed manufacturing process for core–shell structured Si@Gr and Si@Gr/C composite particles and resulting anodes, the impacts of Si content and Si particle size on particulate and electrode properties have been investigated. For this purpose, composites with three different Si contents (5, 10, 15 wt.%) and three different Si particle sizes (120, 160, 250 nm) were compared to pristine Gr. It was shown that the prepared Si@Gr composites without carbon coating are not sufficiently stable, which led to the detachment of Si NPs from the surface and the blocking of pores within the anode. Furthermore, a large impact of the particulate structure on the specific surface area (SSA) was found. While an increase in Si content caused a linear increase in SSA, a decrease in Si particle size resulted in an exponential increase. These trends could be theoretically explained by taking the plate-like shape of the Si particles into account, with a diameter to height ratio of 8:1 showing the best correlation with the measured data. A carbon coating was found to be beneficial, because it reduced the SSA to, or even below, the value of pristine Gr. Moreover, the carbon coating helped stabilize the composite particles, so that the detachment and blocking of pores were prevented.

The electrochemical performance of the produced anodes was investigated both in anode half cells and full cells. All full cells showed high initial capacities $>150 \text{ mAh g}^{-1}$ related to the cathode active material and high initial coulombic efficiencies of $>80\%$. For the variation of Si content, both values could be linked to the previously observed changes in SSA. Furthermore, the cells exhibited excellent rate capability, reaching about 75% capacity retention at 1 C and still 50% at 2 C, respectively. At high C-rates, the lower electrode thicknesses of Si anodes enabled higher capacities than Gr and thus demonstrated the ability of using Si anodes for fast charging applications. An increase of 32% in energy density by using 15 wt.% Si instead of pure Gr further underlined the potential of Si containing anodes. The variation in Si particle size showed only minor impact on performance. Nevertheless, a small improvement in capacity retention was also noted at lower Si particle sizes. The carbon coating enabled even better performance, but it was more pronounced in half cells than in full cells.

Even though the long-term performances of the prepared Si@Gr and Si@Gr/C composite anodes are not sufficient for commercial usage, the results of this study advance the understanding of the impact of particulate properties on performance. Besides that, the electrodes were manufactured at the pilot scale and full cells were built, making the results representative under realistic conditions.

Supplementary Materials: The following supporting information can be downloaded at: <https://www.mdpi.com/article/10.3390/batteries9070377/s1>, Figure S1: Primary particle size (measured by ultrasonic extinction) as a function of specific energy input during grinding (V1–V8 relate to separate experiments, all conducted under the same conditions); Figure S2: Thermogravimetric analysis of Si@Gr and Si@Gr/C composite particles with a variation of Si particle size; Figure S3: Normalized capacity of Si@Gr and Si@Gr/C anodes during long-term cycling test (0.5 C) in half cell configuration (normalized to the capacity at 0.1 C before long-term cycling); Figure S4: (a) Relative discharge capacity during long-term cycling at 0.5 C (normalized to the capacity at 0.1 C after rate capability test and before long-term cycling test, cycle 17); (a) Si@Gr with a variation of Si content; (b) Si@Gr and Si@Gr/C with a variation of particle size; Figure S5: SEM images of Si@Gr and Si@Gr/C composite anodes before and after cycling for 123 cycles; (a,b) Gr; (c,d) Si@Gr, 5 wt.% Si, 120 nm; (e,f) Si@Gr, 10 wt.% Si, 120 nm; (g,h) Si@Gr, 15 wt.% Si, 120 nm; (i,j) Si@Gr/C, 10 wt.% Si, 120 nm; Figure S6: Voltage curves at different cycles (all at 0.1 C); (a) Gr; (b) Si@Gr, 5 wt.% Si; (c) Si@Gr, 10 wt.% Si; (d) Si@Gr, 15 wt.% Si; (e) Si@Gr, 160 nm Si; (f) Si@Gr, 250 nm Si; (g) Si@Gr/C, 120 nm Si; (h) Si@Gr/C, 160 nm Si; Figure S7: Specific energy (Wh kg^{-1}) (a) of Si@Gr as a function of Si content for 120 nm Si NP; (b) of Si@Gr and Si@Gr/C as a function of Si particle size for 10 wt.% Si; Table S1: Overview of the anode coating thickness for the different produced electrodes; Thickness of used copper foil: $h_{\text{Si,Cu}} = 10 \mu\text{m}$.

Author Contributions: Conceptualization, J.M.; methodology, J.M.; validation, J.M.; formal analysis, J.M.; investigation, J.M.; resources, J.M.; data curation, J.M.; writing—original draft preparation, J.M.; writing—review and editing, P.M. and A.K.; visualization, J.M.; supervision, P.M. and A.K.; project administration, P.M. and A.K.; funding acquisition, A.K. All authors have read and agreed to the published version of the manuscript.

Funding: This research was funded by the German Federal Ministry of Education and Research (BMBF) and German Projektträger Jülich (PTJ) within the project “LiBEST²”, grant number 03XP0304B.

Data Availability Statement: The data presented in this study are available in this manuscript and the accompanying Supplementary Materials.

Conflicts of Interest: The authors declare no conflict of interest.

References

1. Tarascon, J.M.; Armand, M. Issues and challenges facing rechargeable lithium batteries. *Nature* **2001**, *414*, 359–367. [[CrossRef](#)]
2. McDowell, M.T.; Lee, S.W.; Nix, W.D.; Cui, Y. 25th anniversary article: Understanding the lithiation of silicon and other alloying anodes for lithium-ion batteries. *Adv. Mater. Weinheim* **2013**, *25*, 4966–4985. [[CrossRef](#)] [[PubMed](#)]
3. Obrovac, M.N.; Christensen, L. Structural Changes in Silicon Anodes during Lithium Insertion/Extraction. *Electrochem. Solid-State Lett.* **2004**, *7*, A93. [[CrossRef](#)]
4. Beaulieu, L.Y.; Eberman, K.W.; Turner, R.L.; Krause, L.J.; Dahn, J.R. Colossal Reversible Volume Changes in Lithium Alloys. *Electrochem. Solid-State Lett.* **2001**, *4*, A137. [[CrossRef](#)]
5. Beaulieu, L.Y.; Hatchard, T.D.; Bonakdarpour, A.; Fleischauer, M.D.; Dahn, J.R. Reaction of Li with Alloy Thin Films Studied by In Situ AFM. *J. Electrochem. Soc.* **2003**, *150*, A1457. [[CrossRef](#)]
6. Yang, Y.; Ni, C.; Gao, M.; Wang, J.; Liu, Y.; Pan, H. Dispersion-strengthened microparticle silicon composite with high anti-pulverization capability for Li-ion batteries. *Energy Storage Mater.* **2018**, *14*, 279–288. [[CrossRef](#)]
7. Wang, J.; Wang, X.; Liu, B.; Lu, H.; Chu, G.; Liu, J.; Guo, Y.-G.; Yu, X.; Luo, F.; Ren, Y.; et al. Size effect on the growth and pulverization behavior of Si nanodomains in SiO anode. *Nano Energy* **2020**, *78*, 105101. [[CrossRef](#)]
8. Winter, M. The Solid Electrolyte Interphase—The Most Important and the Least Understood Solid Electrolyte in Rechargeable Li Batteries. *Z. Für. Phys. Chem.* **2009**, *223*, 1395–1406. [[CrossRef](#)]
9. Schweidler, S.; de Biasi, L.; Schiele, A.; Hartmann, P.; Brezesinski, T.; Janek, J. Volume Changes of Graphite Anodes Revisited: A Combined Operando X-ray Diffraction and In Situ Pressure Analysis Study. *J. Phys. Chem. C* **2018**, *122*, 8829–8835. [[CrossRef](#)]
10. Kim, J.; Chae, O.B.; Lucht, B.L. Perspective—Structure and Stability of the Solid Electrolyte Interphase on Silicon Anodes of Lithium-ion Batteries. *J. Electrochem. Soc.* **2021**, *168*, 30521. [[CrossRef](#)]
11. Wetjen, M.; Pritzl, D.; Jung, R.; Solchenbach, S.; Ghadimi, R.; Gasteiger, H.A. Differentiating the Degradation Phenomena in Silicon-Graphite Electrodes for Lithium-Ion Batteries. *J. Electrochem. Soc.* **2017**, *164*, A2840–A2852. [[CrossRef](#)]
12. Holtstiege, F.; Wilken, A.; Winter, M.; Placke, T. Running out of lithium? A route to differentiate between capacity losses and active lithium losses in lithium-ion batteries. *Phys. Chem. Chem. Phys.* **2017**, *19*, 25905–25918. [[CrossRef](#)] [[PubMed](#)]
13. Pollak, E.; Salitra, G.; Baranchugov, V.; Aurbach, D. In Situ Conductivity, Impedance Spectroscopy, and Ex Situ Raman Spectra of Amorphous Silicon during the Insertion/Extraction of Lithium. *J. Phys. Chem. C* **2007**, *111*, 11437–11444. [[CrossRef](#)]
14. Ryu, J.; Hong, D.; Lee, H.-W.; Park, S. Practical considerations of Si-based anodes for lithium-ion battery applications. *Nano Res.* **2017**, *10*, 3970–4002. [[CrossRef](#)]
15. Wu, H.; Cui, Y. Designing nanostructured Si anodes for high energy lithium ion batteries. *Nano Today* **2012**, *7*, 414–429. [[CrossRef](#)]
16. Luo, Z.; Fan, D.; Liu, X.; Mao, H.; Yao, C.; Deng, Z. High performance silicon carbon composite anode materials for lithium ion batteries. *J. Power Sources* **2009**, *189*, 16–21. [[CrossRef](#)]
17. Zhu, G.; Wang, Y.; Yang, S.; Qu, Q.; Zheng, H. Correlation between the physical parameters and the electrochemical performance of a silicon anode in lithium-ion batteries. *J. Mater.* **2019**, *5*, 164–175. [[CrossRef](#)]
18. Wang, J.; Gao, C.; Yang, Z.; Zhang, M.; Li, Z.; Zhao, H. Carbon-coated mesoporous silicon shell-encapsulated silicon nano-grains for high performance lithium-ion batteries anode. *Carbon* **2022**, *192*, 277–284. [[CrossRef](#)]
19. Liu, X.H.; Zhong, L.; Huang, S.; Mao, S.X.; Zhu, T.; Huang, J.Y. Size-dependent fracture of silicon nanoparticles during lithiation. *ACS Nano* **2012**, *6*, 1522–1531. [[CrossRef](#)]
20. McDowell, M.T.; Ryu, I.; Lee, S.W.; Wang, C.; Nix, W.D.; Cui, Y. Studying the kinetics of crystalline silicon nanoparticle lithiation with in situ transmission electron microscopy. *Adv. Mater. Weinheim* **2012**, *24*, 6034–6041. [[CrossRef](#)]
21. Dimov, N.; Kugino, S.; Yoshio, M. Mixed silicon-graphite composites as anode material for lithium ion batteries. *J. Power Sources* **2004**, *136*, 108–114. [[CrossRef](#)]
22. Lai, S.Y.; Knudsen, K.D.; Sejersted, B.T.; Ulvestad, A.; Mæhlen, J.P.; Koposov, A.Y. Silicon Nanoparticle Ensembles for Lithium-Ion Batteries Elucidated by Small-Angle Neutron Scattering. *ACS Appl. Energy Mater.* **2019**, *2*, 3220–3227. [[CrossRef](#)]
23. Xu, K.; Liu, X.; Guan, K.; Yu, Y.; Lei, W.; Zhang, S.; Jia, Q.; Zhang, H. Research Progress on Coating Structure of Silicon Anode Materials for Lithium-Ion Batteries. *ChemSusChem* **2021**, *14*, 5135–5160. [[CrossRef](#)]

24. Müller, J.; Abdollahifar, M.; Doose, S.; Michalowski, P.; Wu, N.-L.; Kwade, A. Effects of carbon coating on calendered nano-silicon graphite composite anodes of LiB. *J. Power Sources* **2022**, *548*, 232000. [[CrossRef](#)]
25. Liu, W.; Xu, H.; Qin, H.; Lv, Y.; Wang, F.; Zhu, G.; Lin, F.; Wang, L.; Ni, C. The effect of carbon coating on graphite@nano-Si composite as anode materials for Li-ion batteries. *J. Solid State Electrochem.* **2019**, *23*, 3363–3372. [[CrossRef](#)]
26. Tan, W.; Yang, F.; Lu, Z.; Xu, Z. A Design Strategy of Carbon Coatings on Silicon Nanoparticles as Anodes of High-Performance Lithium-Ion Batteries. *ACS Appl. Energy Mater.* **2022**, *5*, 12143–12150. [[CrossRef](#)]
27. Chen, Z.; Zhang, Q.; Liang, Q. Carbon-Coatings Improve Performance of Li-Ion Battery. *Nanomaterials* **2022**, *12*, 1936. [[CrossRef](#)]
28. Müller, J.; Abdollahifar, M.; Vinograd, A.; Nöske, M.; Nowak, C.; Chang, S.-J.; Placke, T.; Haselrieder, W.; Winter, M.; Kwade, A.; et al. Si-on-Graphite fabricated by fluidized bed process for high-capacity anodes of Li-ion batteries. *Chem. Eng. J.* **2021**, *407*, 126603. [[CrossRef](#)]
29. Son, Y.; Kim, N.; Lee, T.; Lee, Y.; Ma, J.; Chae, S.; Sung, J.; Cha, H.; Yoo, Y.; Cho, J. Calendering-Compatible Macroporous Architecture for Silicon-Graphite Composite toward High-Energy Lithium-Ion Batteries. *Adv. Mater.* **2020**, *32*, e2003286. [[CrossRef](#)] [[PubMed](#)]
30. Casino, S.; Niehoff, P.; Börner, M.; Winter, M. Protective coatings on silicon particles and their effect on energy density and specific energy in lithium ion battery cells: A model study. *J. Energy Storage* **2020**, *29*, 101376. [[CrossRef](#)]
31. Andersen, H.F.; Foss, C.E.L.; Voje, J.; Tronstad, R.; Mokkelbost, T.; Vullum, P.E.; Ulvestad, A.; Kirkengen, M.; Mæhlen, J.P. Silicon-Carbon composite anodes from industrial battery grade silicon. *Sci. Rep.* **2019**, *9*, 14814. [[CrossRef](#)]
32. Hsu, Y.-C.; Hsieh, C.-C.; Liu, W.-R. Synthesis of double core-shell carbon/silicon/graphite composite anode materials for lithium-ion batteries. *Surf. Coat. Technol.* **2020**, *387*, 125528. [[CrossRef](#)]
33. Li, P.; Hwang, J.-Y.; Sun, Y.-K. Nano/Microstructured Silicon-Graphite Composite Anode for High-Energy-Density Li-Ion Battery. *ACS Nano* **2019**, *13*, 2624–2633. [[CrossRef](#)]
34. Chae, S.; Choi, S.-H.; Kim, N.; Sung, J.; Cho, J. Integration of Graphite and Silicon Anodes for the Commercialization of High-Energy Lithium-Ion Batteries. *Angew. Chem. Int. Ed. Engl.* **2020**, *59*, 110–135. [[CrossRef](#)]
35. Yang, Z.; Kim, M.; Yu, L.; Trask, S.E.; Bloom, I. Chemical Interplay of Silicon and Graphite in a Composite Electrode in SEI Formation. *ACS Appl. Mater. Interfaces* **2021**, *13*, 56073–56084. [[CrossRef](#)]
36. Moyassari, E.; Roth, T.; Kücher, S.; Chang, C.-C.; Hou, S.-C.; Spangler, F.B.; Jossen, A. The Role of Silicon in Silicon-Graphite Composite Electrodes Regarding Specific Capacity, Cycle Stability, and Expansion. *J. Electrochem. Soc.* **2022**, *169*, 10504. [[CrossRef](#)]
37. Ghalmouche, A.; Müller, M.; Jeschull, F.; Maibach, J. Degradation Phenomena in Silicon/Graphite Electrodes with Varying Silicon Content. *J. Electrochem. Soc.* **2022**, *169*, 20541. [[CrossRef](#)]
38. Nöske, M.; Breitung-Faes, S.; Kwade, A. Electrostatic Stabilization and Characterization of Fine Ground Silicon Particles in Ethanol. *Silicon* **2019**, *574*, 20. [[CrossRef](#)]
39. Froboese, L.; Titscher, P.; Westphal, B.; Haselrieder, W.; Kwade, A. Mercury intrusion for ion- and conversion-based battery electrodes—Structure and diffusion coefficient determination. *Mater. Charact.* **2017**, *133*, 102–111. [[CrossRef](#)]
40. Haselrieder, W.; Westphal, B.; Bockholt, H.; Diener, A.; Höft, S.; Kwade, A. Measuring the coating adhesion strength of electrodes for lithium-ion batteries. *Int. J. Adhes. Adhes.* **2015**, *60*, 1–8. [[CrossRef](#)]
41. Morasch, R.; Landesfeind, J.; Suthar, B.; Gasteiger, H.A. Detection of Binder Gradients Using Impedance Spectroscopy and Their Influence on the Tortuosity of Li-Ion Battery Graphite Electrodes. *J. Electrochem. Soc.* **2018**, *165*, A3459–A3467. [[CrossRef](#)]
42. Park, M.; Zhang, X.; Chung, M.; Less, G.B.; Sastry, A.M. A review of conduction phenomena in Li-ion batteries. *J. Power Sources* **2010**, *195*, 7904–7929. [[CrossRef](#)]

Disclaimer/Publisher’s Note: The statements, opinions and data contained in all publications are solely those of the individual author(s) and contributor(s) and not of MDPI and/or the editor(s). MDPI and/or the editor(s) disclaim responsibility for any injury to people or property resulting from any ideas, methods, instructions or products referred to in the content.